Journal of Materials Chemistry A

ROYAL SOCIETY OF CHEMISTRY

PAPER

View Article Online
View Journal | View Issue

Published on 20 November 2023. Downloaded by Texas A & M University on 6/3/2024 5:10:04 PM.

Check for updates

Cite this: *J. Mater. Chem. A*, 2023, **11**, 26252

PTFE nanocoating on Cu nanoparticles through dry processing to enhance electrochemical conversion of CO_2 towards multi-carbon products†

John Pellessier, ‡[a] Xiangtao Gong, ‡[a] Boyang Li,[b] Jiaqi Zhang,[c] Yang Gang,[a] Kirk Hambleton,[a] Chinmoy Podder,[a] Zhongjia Gao,[a] Hongcai Zhou,[c] Guofeng Wang,[b] Heng Pan *[a] and Ying Li *[a]

Received 23rd September 2023
Accepted 20th November 2023

DOI: 10.1039/d3ta05787a

rsc.li/materials-a

Polymer modified copper (Cu) catalysts have demonstrated an increased production of multi-carbon (C_{2+}) products during the electrochemical CO_2 reduction reaction (CO_2RR). Herein, a solvent-free processing method has been developed to cover commercial Cu nanoparticles with a porous nanocoating of polytetrafluoroethylene (PTFE) that greatly improved the production of C_{2+} products. The PTFE coating created a large interfacial surface area that facilitated the transport of CO_2 to the solid–liquid–gas interface. The optimal catalyst achieved a faradaic efficiency of 78% for C_{2+} products and a notably large C_{2+} to C_1 product ratio of ~13 at current densities ranging from 400 to 500 mA cm^{-2}. In comparison, catalysts prepared by a conventional solvent-based method only achieved a faradaic efficiency of 56% for C_{2+} products and a small C_{2+} to C_1 product ratio of ~2 in the same current density range. Density functional theory (DFT) calculations suggested that the physisorbed PTFE coating on Cu catalysts plays a more significant role than the most frequently studied chemisorbed PTFE. The physisorbed PTFE is predicted to increase the binding energy of CO intermediates on Cu and lower the activation energy for C–C coupling steps, leading to significantly higher C_{2+} product selectivity of the Cu catalysts.

Introduction

Carbon dioxide (CO_2) can be converted into value-added chemicals and fuels *via* the electrochemical carbon dioxide reduction reaction (CO_2RR).[1–3] In recent years researchers have reported in abundance on catalysts for the production of single-carbon (C_1) products.[4–11] However, there are increasing interests in the field of CO_2RR to produce multi-carbon (C_{2+}) products that have higher market values.[12–14] Currently, copper (Cu) is the most prominent metal catalyst that can facilitate the formation of C–C bonds; however, the selectivity for C_{2+} products on untreated Cu is low. As such, most research into producing C_{2+} products from CO_2 is focused on altering or modifying Cu such as the oxidation state, exposed facets, and morphology, or by creating bimetallic alloys with Cu.[12,15–29] One such technique for modifying Cu that remained underexplored until recent years is the polymer modification on the Cu surface or integration of polymer into a Cu based catalyst layer. While many cathode systems already contain polymers such as Nafion or polytetrafluoroethylene (PTFE) in some form, the role they provide is commonly limited to acting as a binder, providing structural support as the substrate for the catalyst, or increasing hydrophobicity of the cathode.[4,30,31]

The effect a polymer–Cu interface has on promoting C_{2+} production has been increasingly reported by experimental and computational studies. The results indicate that surface modification of Cu by polymers containing oxygen, nitrogen, or fluorine functional groups not only increases the hydrophobicity of the cathode, but also can suppress the competing hydrogen evolution reaction (HER) and help boost C_{2+} product selectivity through stabilization of the reaction intermediates.[32–37] For instance, Wei *et al.* coated Cu foil with polyaniline and demonstrated increase of C_{2+} product selectivity from 15% to 60% and the reason was ascribed to the increase of intermediate CO coverage on Cu.[34] Wang *et al.* found that polymer addition lowered the energy barrier for CO protonation from 1.14 eV to 0.68 eV despite an increase in ohmic resistance.[36] García de Arquer *et al.* created a catalyst/ionomer interface to facilitate the transport of reactant, product, and electron, which resulted in a 67% C_{2+} product selectivity under a 510 mA cm^{-2} current density.[33] Only a few theoretical studies have been conducted to understand the effect of polymer coating on the C_{2+} product selectivity. Chang

[a]*J. Mike Walker '66, Department of Mechanical Engineering, Texas A & M University, College Station, Texas 77843, USA. E-mail: yingli@tamu.edu; hpan@tamu.edu*

[b]*Department of Mechanical Engineering and Materials Science, University of Pittsburgh, Pittsburgh, Pennsylvania 15261, USA*

[c]*Department of Chemistry, Texas A & M University, College Station, Texas 77843, USA*

† Electronic supplementary information (ESI) available. See DOI: https://doi.org/10.1039/d3ta05787a

‡ These authors contributed equally.

This journal is © The Royal Society of Chemistry 2023

Published on 20 November 2023. Downloaded by Texas A & M University on 6/3/2024 5:10:04 PM.

et al. explored the surface modification of Cu with polymer functional groups such as –COOH and $–CF_2$ and found the functional groups influence the binding energies of key intermediates involved in CO_2RR.[35] Ahn *et al.* revealed that a poly(-acrylamide)–Cu interface enhanced ethylene formation through charge donation, but their model involved an acrylamide monomer as being chemisorbed onto Cu.[38] Those literature studies modeling the interface only used a single functional group or a single monomer of their chosen polymer on Cu, which is not always an accurate representation of a polymer–Cu interaction, especially in the case of a physically adsorbed polymer.

Other than the importance of creating active and selective interfaces at an atomic level by polymer modification for optimal CO_2RR performance, the controllable and sustainable fabrication of a catalyst layer with desired structure from micro to macro scales is vital. Currently, most reported methods to prepare a polymer–Cu interface and resultant working electrode utilize excessive amounts of solvents.[33,34,36] Catalyst ink coating is currently the most common fabrication method for preparing the working electrode. Most inks are prepared by dispersing catalyst nanoparticles in isopropanol/water mixture and coated by air brushing or ultrasonic spraying coating.[33,36,39–41] However, insufficient ink stability, inhomogeneous catalyst layers and uncontrollable structures due to complex catalyst dispersion and solvent drying processes are common problems.[42] New methods allowing the controllable fabrication of catalyst layers across different scales simultaneously, thereby bridging interface engineering and sustainable manufacturing, are highly desirable.

In this study, for the first-time, a solvent-free process is developed to manufacture electrodes by modifying commercial Cu nanoparticles (NPs) with a nanofilm of PTFE and dry coating the PTFE modified Cu nanoparticles as a catalyst layer for CO_2RR. This new method avoids complex preparation processes and the use of excess amounts of solvents or chemical additives as reported in the literature when applying conventional solvent-based catalyst production methods.[32–35,38,43,44] Thus-fabricated PTFE coated Cu nanoparticles (NPs) aggregated together to form interconnected porous 3D micro-granules, which were dispersed onto a carbon gas diffusion layer (GDL) by electrostatic deposition to form the cathode. Electrochemical tests were conducted in a three-electrode flow cell, where a faradaic efficiency of C_{2+} at 78% and a C_{2+} to C_1 product ratio of 13 were remarkedly achieved at a high current densities ranging from 400 to 500 mA cm^{-2}. The excellent CO_2RR performance is ascribed to a nearly complete surface coverage of the Cu NPs by the porous PTFE film and the creation of large Cu–polymer interfacial area. Moreover, the density functional theory (DFT) calculations were preformed to elaborate on the beneficial effect of physisorbed PTFE coating on the CO_2RR performance of Cu toward C_2 products.

Methods

Chemicals and materials

The up-to-date and widely used commercial copper nanoparticles (NPs, 40 nm) from US Research Nanomaterials, Inc. were adopted as the active materials. Polytetrafluoroethylene (PTFE, free-flowing, 2.15 g mL^{-1}) powders from Sigma-Aldrich were adopted as the polymer. The substrate used for cathode manufacturing was the gas diffusion layer (GDL) Sigracet 39 BC purchased from the Fuel Cell Store. Isopropyl alcohol (IPA, ACS grade) was purchased from VWR. Nafion solution of 5 wt% was purchased from the Fuel Cell Store (D520). Potassium hydroxide (KOH, purity ≥85%) was also purchased from VWR and used along with deionized (DI) water with a resistance of ≥18 MΩ cm to prepare the electrolyte. The materials were used without further purification or treatment.

Materials characterization

Scanning electron microscopy (SEM) images were collected on a JEOL JSM7500F. Transmission electron microscopy (TEM) images were collected on a Tecnai G2 F20 ST FE-TEM operated at 200 kV. To prepare for TEM imaging, 20 μL of the sample was dispersed into IPA which was then dropped onto a 400-copper mesh grid (Electron Microscopy Sciences). X-ray photoelectron spectroscopy (XPS) was collected on an Omicron using a dual Mg/Al X-ray source. Brunauer–Emmett–Teller (BET) surface area analysis was collected on a Micromeritics ASAP 2420 physisorption analyzer. X-ray diffraction (XRD) patterns were collected on a BRIKER D8.

Preparation of working electrode *via* DRY method

The granules were prepared by loading Cu and PTFE in powder form into the ball-milling chamber with milling balls. The resulting Cu/PTFE granules were loaded in the hopper for dry electrostatic spray, the granules were evenly distributed on the GDL with a loading of 1 mg cm^{-2}. Following deposition roller pressing was used to improve the bonding.

Preparation of working electrode *via* WET method

The comparison wet method electrode was prepared by air-brushing a catalyst ink onto the GDL. The Cu/Nafion ink consisted of 10 mg Cu, 55 μL of 5 wt% Nafion solution, and 2 mL IPA which had been sonicated for one hour. The Cu/PTFE ink consisted of 28.8 mg Cu, 7.2 mg PTFE, and 6 mL IPA which had been sonicated for one hour. An accurate loading of 1 mg of catalyst per 1 cm^2 ± 0.1 mg was achieved by comparing the initial weight of the GDL to the weight during and after catalyst deposition. The cathode was then placed into a vacuum oven overnight to dry after which the weight was once again checked.

Results and discussion

Materials design and innovation

Fig. 1a and b show schematic illustrations and corresponding SEM images of the Cu–PTFE catalyst systems prepared through (a) conventional airbrushing of a catalyst ink made of Cu–PTFE mixture (WET) and (b) solvent-free dry processing method to coat PTFE on Cu (DRY). The morphologies of the raw Cu and PTFE NPs are shown in Fig. S1,† which reveals that Cu NPs are nearly spherical with an average size of 50 to 100 nm and the PTFE NPs are oval shaped with an average size of 100 to 200 nm. From

Published on 20 November 2023. Downloaded by Texas A & M University on 6/3/2024 5:10:04 PM.

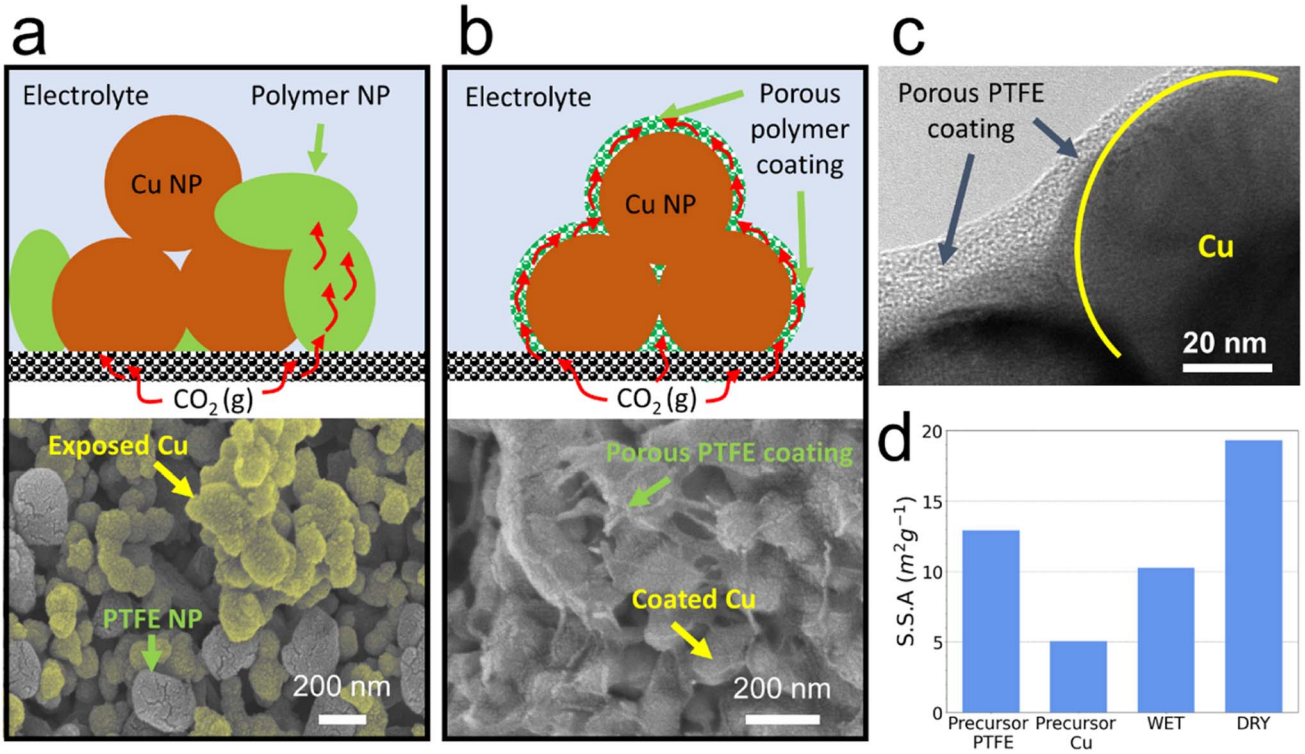

Fig. 1 Schematic illustrations and SEM images of a Cu–PTFE catalyst layer on gas diffusion electrode (GDE) made of (a) simple mixture of Cu and PTFE nanoparticles through air-brushing the catalyst ink (WET) where Cu has been highlighted yellow, (b) PTFE nanofilm coated Cu through dry processing (DRY) that facilitates CO_2 transport; (c) TEM image of DRY sample showing the PTFE nanocoating on Cu; (d) the BET specific surface areas of the precursor materials and the WET and DRY catalysts.

Fig. 1a, the WET method does not cause any changes in the morphology of the two raw materials in the final catalyst containing 80 wt% Cu and 20 wt% PTFE (named WET/20%PTFE). The Cu and PTFE NPs are assembled as a simple mixture and no coating of PTFE on Cu is observed. In contrast, from Fig. 1b, the DRY method results in a nearly complete coverage of PTFE on Cu NPs in the form of nanofilm or nanofiber, for the sample containing 80 wt% Cu and 20 wt% PTFE that underwent a 30 min ball-milling process (named DRY/20%PTFE/30min). The nanocoating is formed when the Cu and PTFE raw powders are mixed and undergone a ball mill process, during which the PTFE NPs easily deform and are coated around the Cu NPs. Note that because of the large size of Cu NPs, the difference in electronic structure and catalytic activities caused by different Cu NP assemblies in the WET and DRY samples is minimal and negligible.

To understand the PTFE coating formation process, SEM images of a DRY/20%PTFE sample were taken during the initial period of ball-milling (0–180 s), as shown in Fig. S2.† After only 20 s, the PTFE NPs started to deform, while the structure of the Cu NPs has not changed. As processing time went on, namely after 120 s, all the PTFE NPs appeared to deform to various extents. After 180 s, the PTFE NPs began to adhere together and started coating Cu. These images confirm that the coating is a result of PTFE deformation, followed by amalgamation of the PTFE, and finally coating and adhesion onto Cu NPs.

Transmission electron microscopy (TEM) images of DRY/20%PTFE/30min were collected to further confirm the coverage of Cu NPs by PTFE. There is no evidence of PTFE coverage on Cu from the TEM images of the WET/20%PTFE samples (Fig. S3†). However, Fig. 1c clearly shows surface coating of the Cu NPs by an ultrathin PTFE film with thickness in the range of 5 to 14 nm on the DRY/20%PTFE/30min sample. An additional TEM image highlighting the PTFE coverage on DRY/20%PTFE/30min can be seen in Fig. S4.†

One advantage of the PTFE coated Cu is evidenced from the specific surface area (S.S.A) of the catalyst measured by the Brunauer–Emmett–Teller (BET) method. As shown in Fig. 1d, the raw PTFE and Cu NPs had an S.S.A. of 12.5 $m^2\ g^{-1}$ and 5.0 $m^2\ g^{-1}$, respectively. The WET/20%PTFE sample had an S.S.A. slightly over 10 $m^2\ g^{-1}$, representing the mixture of the two raw materials without morphology changes. Interestingly, the DRY/20%PTFE/30min sample had an S.S.A of nearly 20 $m^2\ g^{-1}$, far greater than those of the individual precursor materials and WET/20%PTFE. This larger S.S.A indicates increased porosity attributed to the morphology change of PTFE and formation of PTFE overcoating during the dry processing. As a result of the PTFE coverage and increased porosity on the DRY sample, a larger area of catalyst–electrolyte–gas interface on the gas diffusion electrode is created and the reactant gas (CO_2) is more readily transported to those interfaces, as illustrated in Fig. 1b.

Fabrication and characterization of Cu–PTFE micro-granules and the gas diffusion electrode

A variety of Cu–PTFE catalysts were fabricated by varying the PTFE mass loading and ball milling time, and correlation of

 This journal is © The Royal Society of Chemistry 2023

Published on 20 November 2023. Downloaded by Texas A & M University on 6/3/2024 5:10:04 PM.

synthesis parameters and resultant morphology of PTFE coated Cu micro-granules is explored. The prepared samples were named DRY/X%PTFE/Ymin, where X and Y represent the mass percentage of PTFE in the Cu–PTFE composite and ball milling time, respectively. The SEM images of DRY/20%PTFE/Ymin samples processed with different periods of ball milling time (Y = 0–30 min) are shown in Fig. S5 and S6.† The uniformity of the micro-granules in terms of size and morphology increased with the ball milling time. At times less than 15 min, a uniform PTFE coating was not achieved. At 15 min, some uncoated Cu NPs can still be seen despite a relatively uniform coating was observed. At 30 min, no exposed Cu NPs on the micro-granule surfaces were observed. The SEM images of DRY/X%PTFE/30min samples with different PTFE mass loading (X = 2%, 20%, and 50%) are shown in Fig. S7.† The PTFE coverage and coating thickness increased as PTFE mass loading increased, with no sufficient coverage at 2% while too thick a coating at 50%, and a more balanced coverage and coating thickness at 20% PTFE mass loading. Of note from these images is that regardless of PTFE mass loading, enough ball milling time (*e.g.*, 30 min) resulted in similar sizes of micro-granules. These results indicate that the micro-granule size, shape, and surface morphology are dependent on both the ball milling time and the PTFE mass loading.

After the Cu–PTFE micro-granules were formed in the ball mill processing, it was attempted to deposit them on a GDL to form a GDE. Because of the relatively large size of the micro-granules, typically in a few micrometers as shown in Fig. 2a, conventional methods including airbrushing or drop casting the micro-granules on GDL were unsuccessful. Alternatively, an electrostatic spray distribution (ESD) method was used to distribute the micro-granules onto the GDL to form a GDE. This is the first time this method has been reported for preparing CO_2RR catalyst layered on a GDL. The whole manufacturing process, from Cu–PTFE catalyst to cathode preparation, is thus solvent free. The workflow to manufacture the GDE is shown in Fig. 2b. The catalyst micro-granules were loaded into the hopper, sprayed out of the charged spray gun nozzle, and deposited on the GDL, which was placed on an electronically grounded plate holder. These charged micro-granules were attracted to the grounded GDL forming a well-dispersed layer. A photo of a fabricated GDE (2 cm × 3 cm) and SEM images from the top view and cross section view of the GDE are shown in Fig. 2c, where a single layer of micro-granule deposition is observed. The mass loading of the micro-granules can be controlled by varying the spray time. Next, the micro-granule-coated GDL was passed through a set of rollers to improve granule-GDL bonding. For future large-scale manufacturing, a roll-to-roll method integrating the dry spraying and roll-pressing steps can be realized (see Fig. S8†).

To investigate the internal structure and morphology, a micro-granule was cut by a focused ion beam (FIB), and an SEM image of the micro-granule cross-section is shown in Fig. 2d. The fibrous and film-like PTFE coating is also found in the cross-section of the micro-granule like those seen on the outer surface of the micro-granule (Fig. 1c and S6, S7†). All the NPs seen in the cross-section FIB images are likely Cu NPs that are connected by PTFE overcoating, forming an interconnected porous structure within the Cu–PTFE micro-granule.

The SEM and energy dispersive spectroscopy (EDS) elemental mapping of the micro-granules on an as-prepared cathode are shown in Fig. 2e–g. Cu elements are only found on the micro-granules, whereas F is found elsewhere besides the micro-granules. Fluorine is an indication of the presence of PTFE, and its appearance outside of the micro-granule is because the commercial GDL used contains a thin layer of PTFE coating on its microporous layer. The EDS analysis (Fig. S9a†) estimated a Cu : F weight ratio of 4.9 for the DRY/20%PTFE/30min micro-granule, matching the nominal of 5.3 expected from the 4 : 1 ratio used in the preparation recipe. On the other hand, the EDS analysis of the WET/20%PTFE sample (Fig. S9b†) shows Cu and PTFE co-exist as individual nanoparticles without any coating.

The morphology differences between the GDEs prepared by the WET and DRY methods are evidenced by the cross-section SEM images of the GDEs as shown in Fig. 2c (DRY) and Fig. S10† (WET). The WET/20%PTFE GDE has a continuous, smooth catalyst layer (~4 μm in thickness) made of a mixture of Cu and PTFE NPs completely covering the microporous layer of the GDL, while the DRY/20%PTFE/30min GDE has a rougher, slightly thicker (5–10 μm, depending on the size of micro-granule), and less evenly distributed catalyst layer coating on the GDL because of the irregular structure of the micro-granules.

This higher surface roughness of the DRY-method prepared cathode appeared to enhance the hydrophobicity of the GDE compared to the WET-method prepared one. As evidenced by the water contact angles reported in Fig. 3a, b and Table S1,† all cathodes prepared *via* the DRY method had contact angles around 145° (with uncertainty of ±2°) suggesting a high hydrophobicity. The WET/20%PTFE cathode only had a contact angle of 115°, indicating a lower-level hydrophobicity.

X-ray photoelectron spectroscopy (XPS) was utilized to explore the surface chemical composition of the various catalysts. From the full range XPS analyses and high resolution XPS analyses of F 1s and Cu 2p peaks (Fig. S11†), the Cu and F surface weight percentages are calculated and shown in Fig. 3c. The WET/20%PTFE sample had a much higher weight percentage of Cu on it than DRY/20%PTFE/30min had, indicating much more exposed Cu on the surface of the WET/20% PTFE sample, matching the morphology differences observed from the previous SEM and TEM analyses. For the DRY samples with various PTFE contents, as the PTFE content increased from 5% to 20% and to 35%, the absolute Cu weight content dropped to lower than about 1% when the PTFE mass loading was 20% or higher. Because XPS is a surface analysis technique sensitive to up to 10 nm below the surface, this XPS result confirms that the Cu NPs are almost completely coated by PTFE for the DRY samples containing PTFE content at 20% and above. As is comparatively evidenced in Fig. S11† at 0 to 30 s of ball milling time increased the Cu 2p peaks are still evident, indicating the ball milling process is responsible for applying the PTFE coating. It should be noted that XPS analyses indicate the absence of CuO in the catalyst, evidenced by the main Cu $2p_{3/2}$

Published on 20 November 2023. Downloaded by Texas A & M University on 6/3/2024 5:10:04 PM.

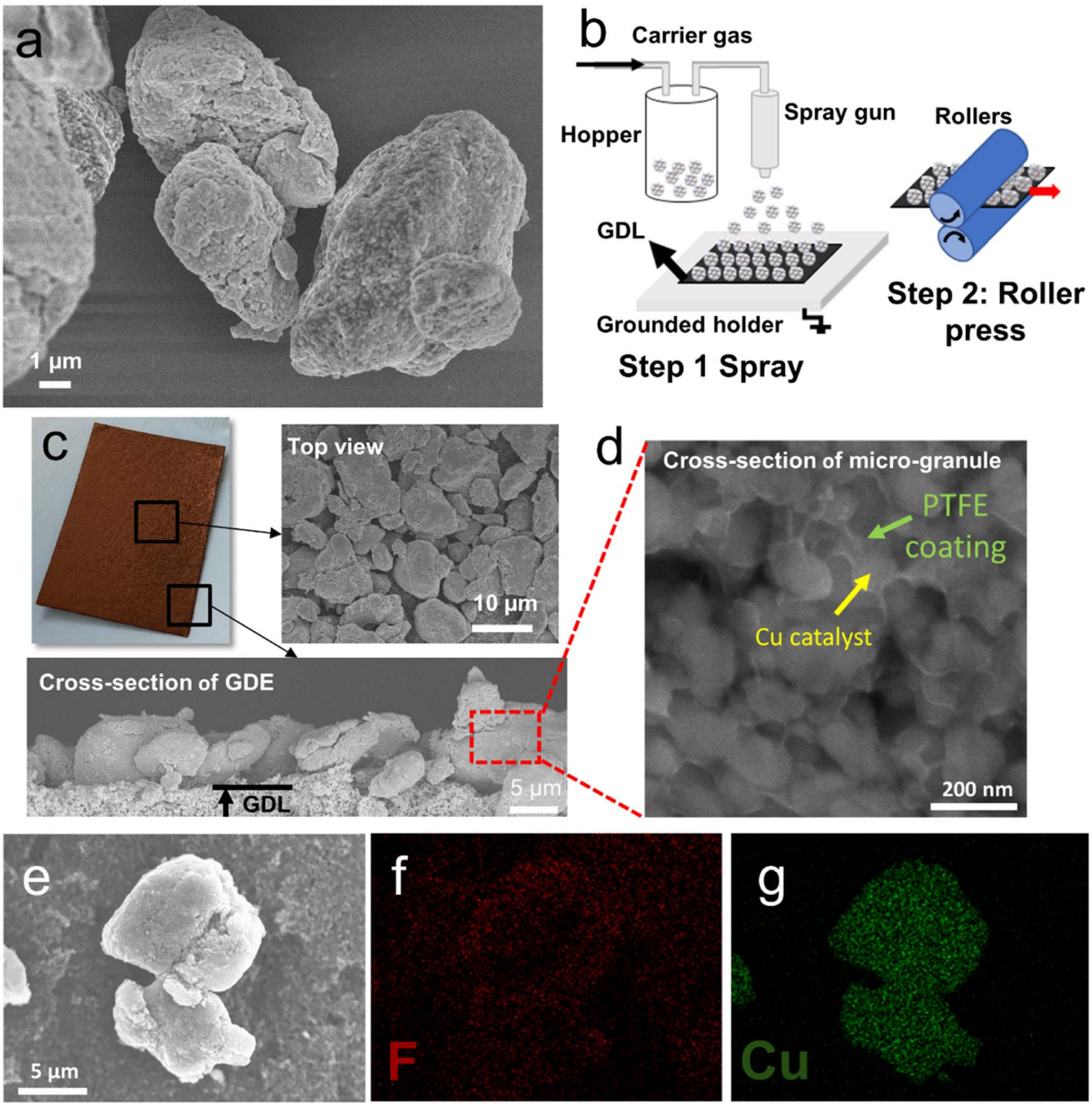

Fig. 2 (a) SEM image of prepared micro-granules. (b) Graphical representation of the electrostatic spray and roller press to fabricate the GDE. (c) A typical completed cathode with SEM images from a top view and a cross section view. (d) FIB-SEM cross-section image of a micro-granule. (e–g) EDS elemental mappings of the micro-granule deposited onto a GDL *via* EDS.

peaks not being shifted and by the absence of satellite peaks which would appear around 942 eV and 962 eV.[45]

While XPS results show a significant covering of Cu by PTFE in the DRY samples, the double layer capacitance (C_{dl}) and by extension the electrochemical surface area (ECSA) of DRY/20% PTFE/30min were analyzed to understand the accessibility of electrolyte to the DRY sample. As shown in Fig. S12,† the C_{dl} of DRY/20%PTFE/30min was 1.37 mF cm^{-2}, smaller than that of WET/20%PTFE (4.02 mF cm^{-2}). The decreased current density of DRY compared to WET samples at similar potentials in Fig. S12† is directly related to the loss in ECSA. The lost ESCA is most likely ascribed to the relatively large size (a few micrometers) and more hydrophobic DRY granules, making it more difficult for Cu nanoparticles in the center of the granule to contact the electrolyte. However, the DRY sample is still reasonably accessible to electrolyte despite the PTFE coverage, which can be attributed to its porous structure as evidenced by the increased specific surface area of DRY over WET sample (Fig. 1d). Future research will investigate the fabrication of smaller granules to improve the ECSA of DRY samples.

 This journal is © The Royal Society of Chemistry 2023

Published on 20 November 2023. Downloaded by Texas A & M University on 6/3/2024 5:10:04 PM.

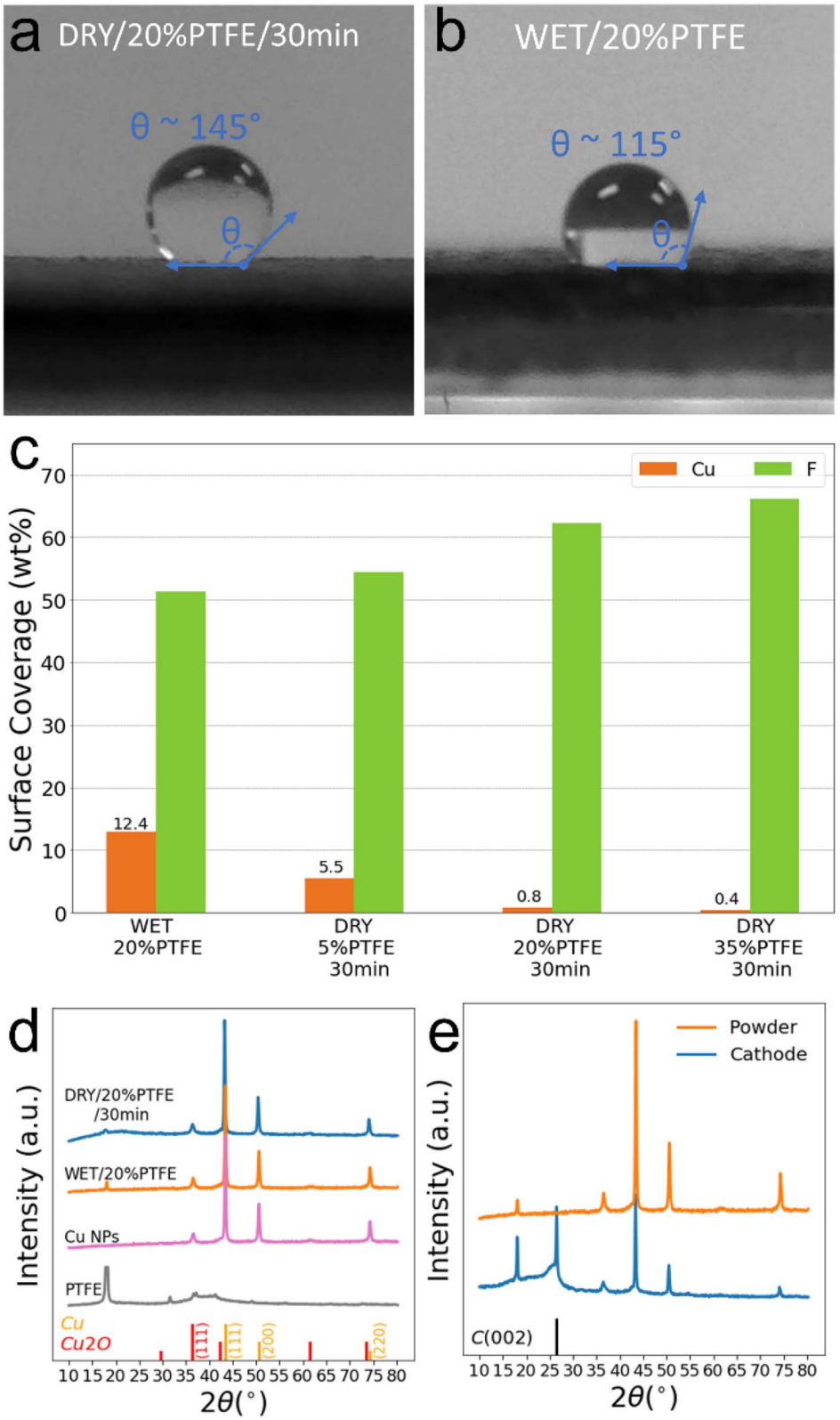

Fig. 3 Water contact angle measured on the cathode made of (a) DRY/20%PTFE/30min and (b) WET/20%PTFE; (c) surface elemental composition of Cu and F on various catalysts as determined by XPS; (d) XRD patterns of precursor materials, DRY/20%PTFE/30min, and WET/20% PTFE; (e) XRD patterns comparing DRY/20%PTFE/30min catalyst and the resultant cathode.

Published on 20 November 2023. Downloaded by Texas A & M University on 6/3/2024 5:10:04 PM.

The crystal structures of the catalysts were investigated by X-ray diffraction (XRD) as shown in Fig. 3d. The diffraction peaks in the prepared catalysts matched up with peaks of the individual precursor Cu NPs and PTFE powders. The peak at 17° is assigned to PTFE. The Cu peaks for Cu NPs, WET/20%PTFE, and DRY/20% PTFE/30min are almost identical, suggesting that the ball milling process did not alter the crystal structure of the Cu catalyst. Those Cu peaks correspond to facets of Cu (111), (200), and (220) at 43.7°, 50.7°, and 74.3° respectively. A small peak at 36.4° may be evident of a trace amount of Cu_2O (111). No peaks corresponding to CuO are evident in the XRD patterns agreeing with the XPS results. To determine if the electrostatic deposition method used to prepare the cathodes had any effects on the crystal structure, XRD patterns of the DRY/20%PTFE/30min catalyst sample and as-prepared cathode are compared (Fig. 3e). The XRD pattern of the prepared cathode is like that of the catalyst except that the intensity of Cu peaks is lower, the F peaks are stronger due to PTFE on the microporous layer of GDL, and an additional graphite peak (26.5°) due to the carbon fibers in the GDL. These XRD results confirm that the different preparation methods of catalysts and GDEs did not change the crystal structure of the Cu catalyst.

Electrochemical CO_2RR performance

Electrochemical testing of the prepared cathodes was conducted in a three-electrode flow cell. A schematic of the cell is shown in Fig. S13.† All the potentials recorded in this work were reported with solution resistance correction. Two data points were collected for each testing condition reported herein. First, a baseline test was performed by using Ar (instead of CO_2) as the feed gas passing through a Cu–PTFE cathode. As shown in Table S2,† H_2 was the only product and no carbon-containing products were detected in either gas phase or liquid phase. This baseline test confirms that carbon-containing products produced in this work as described later in the paper are from CO_2 not from the carbon substrate (GDL) or PTFE. Complete data on the electrochemical performance of all catalysts (WET and DRY) can be found in Tables S3–S7 in the ESI.†

Initial electrochemical testing was conducted on DRY catalysts to determine how varying the mass percentage of PTFE used in preparing the catalyst and changing the ball milling time would affect the product selectivity at an industrial viable current density (fixed at 200 mA cm^{-2}). As shown in Fig. 4a, for the catalysts prepared at fixed ball milling time (30 min) but varying PTFE contents, the selectivity for C_{2+} products initially increased with the mass loading of PTFE. The catalyst prepared with 20% PTFE obtained a C_{2+} to C_1 ratio of 4.3 with a total FE (C_{2+}) of 71%. The catalyst containing 25% PTFE achieved a larger C_{2+} to C_1 ratio of 6.2 but also showed an increase in selectivity for H_2 and only achieved an FE (C_{2+}) of 60%. An even larger PTFE loading of 35% resulted in a significantly increased selectivity for H_2 and a low FE (C_{2+}) at only 15%. The main C_{2+} products of ethylene and ethanol agree with other reports that the (100) facet in Fig. 3d is favorable for producing C_2H_4 while the (100) × (110) step sites are suspected to favor ethanol production.[16,29,46] As PTFE is an electrical insulator the working potential slightly increased with the higher loadings of PTFE.

The electrochemical performance of catalysts prepared with a fixed mass loading of 20% PTFE but a varied ball milling time in the range from 30 s to 60 min is shown in Fig. 4b. Catalysts processed with a ball milling time of 30 s and 9 min demonstrated almost the same selectivity, while those processed with 15 min showed a slightly higher C_{2+} product selectivity that the previous two. All three catalysts had C_{2+} selectivity less than 60% and C_{2+} to C_1 ratios less than 2. With a ball milling time at 30 min or 60 min, the FE (C_{2+}) significantly increased to more than 70% and the C_{2+} to C_1 ratio increased to more than 4. The catalyst with 60 min ball milling time resulted in negligible changes to the product selectivity compared to those with 30 min. The catalytic performance in terms of C_{2+} selectivity is well correlated with the ball milling time and the resulting surface coverage of PTFE on Cu (Fig. S6†). That is, when there were no fully exposed Cu NPs on the micro-granule surfaces (until 30 min ball milling), the increase in C_{2+} selectivity became significant. Lastly, it is noticed that the overpotential did not increase with the ball milling time (or PTFE coverage), unlike the trend observed for increased PTFE loading. Because in this case the PTFE loading was fixed at 20%, both the PTFE coverage on Cu and Cu/PTFE granule size would affect the catalyst conductivity and thus overpotential. As shown in Fig. S5 and S6,† as mixing time increases from 30 s to 15 min, the Cu/PTFE mixture transitions from large aggregates to smaller, more tightly packed granules, and PTFE transitions from bulky nanoparticles to a uniform and thin film. Because Cu NPs were brought closer together and the thickness of the PTFE coating decreased with ball milling time, the overall resistance of the granules and the overpotential decreased up to 15 min. When the ball milling time was extended to 30 min or more, Cu was almost fully covered by PTFE, causing a slightly increased overpotential.

Next, the performances of catalysts prepared using conventional WET methods were evaluated. Besides WET/20%PTFE, another sample WET/20%Nafion was also prepared by dispersing commercial Cu NPs and a 20% mass loading of Nafion into isopropyl alcohol and airbrushing the resulting catalyst ink onto a GDL. The electrochemical performances of WET/20%Nafion and WET/20%PTFE can be seen in Fig. 5a and b, respectively. WET/20%PTFE had a lower FE (C_{2+}) than WET/20%Nafion at 100 mA cm^{-2} but equivalent or slightly higher FE (C_{2+}) than WET/20%Nafion at 200 mA cm^{-2} or higher current densities. Additionally, WET/20%PTFE showed a better suppression of the competing HER at all current densities and a lower overpotential at high current densities as compared to WET/20%Nafion. This suggests that for flow cell operations at high current densities, the use of PTFE NPs simply as a binder with Cu would contribute to a higher C_{2+} selectivity than the most widely used Nafion binder. This agrees with the literature that the choice of polymeric binder could have a large influence on product selectivity despite varying degrees of hydrophobicity.[33,41,44,47,48]

From the results in Fig. 4 it was determined that the optimal parameters for preparing the PTFE coated Cu NPs are a mass loading of 20% PTFE and a ball milling time of 30 min, *i.e.*, the DRY/20%PTFE/30min sample. Additional experiments using

 This journal is © The Royal Society of Chemistry 2023

Published on 20 November 2023. Downloaded by Texas A & M University on 6/3/2024 5:10:04 PM.

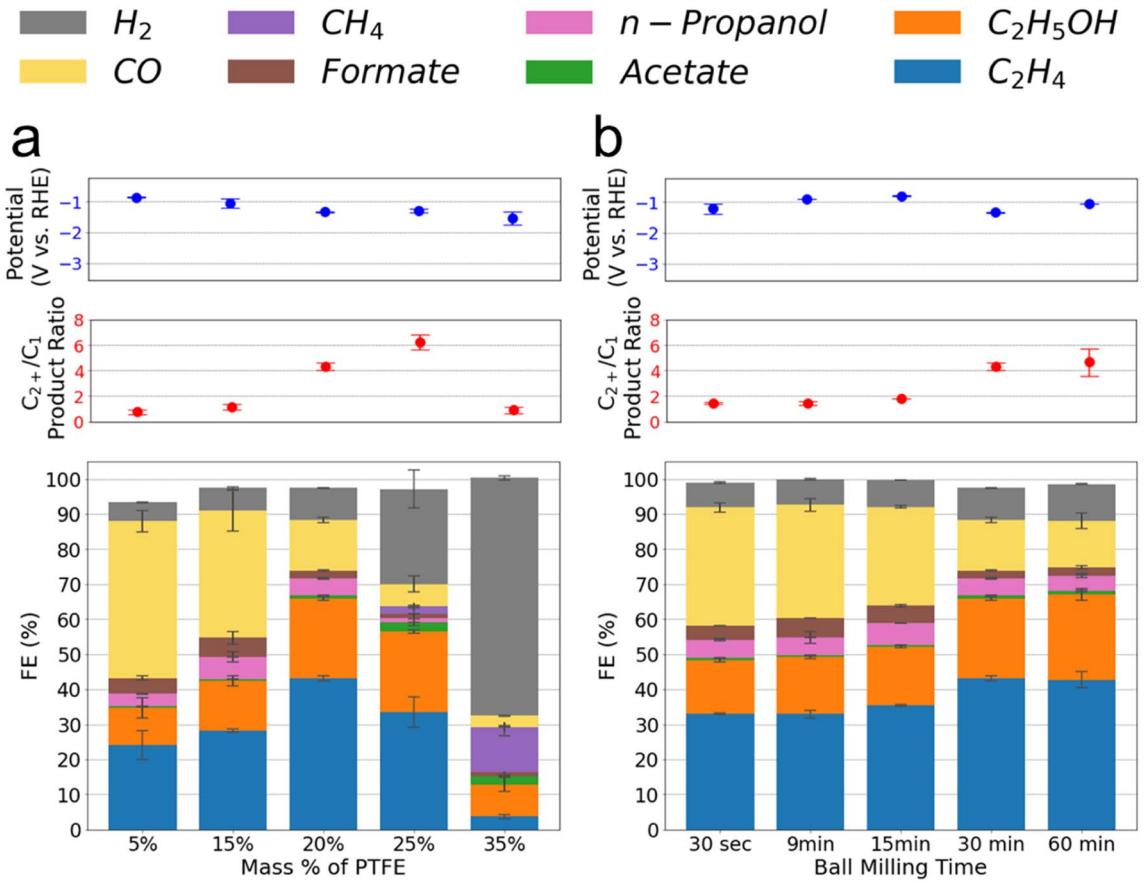

Fig. 4 Effects of (a) PTFE mass loading and (b) ball milling time in catalyst preparation on CO_2RR product faradaic efficiencies, C_{2+}/C_1 product ratio, and working potential, tested in a flow cell at 200 mA cm^{-2}.

this sample were then conducted at different current densities and the performances compared to catalysts prepared using conventional WET methods. Fig. 5c shows the electrochemical performance of DRY/20%PTFE/30min over a range of applied currents. The highest recorded selectivity for C_{2+} products was seen under a current of 400 mA cm^{-2} when a total FE (C_{2+}) of 78% was achieved, where ethylene and ethanol were the two major products with selectivities of 43.3% and 28.4%, respectively. The DRY/20%PTFE/30min catalyst also achieved a remarkably high C_{2+} to C_1 product ratio of 13 at current densities of 500 mA cm^{-2} or greater (Fig. 5d). Comparing the DRY/20%PTFE/30min performance with the literature reported data (Table S8†), this catalyst is among the top performing catalysts in terms of FE (C_{2+}) and/or C_{2+}/C_1 product ratio at high current densities around 400 to 500 mA cm^{-2}. This current density is of importance as it falls within the current range of 200–500 mA cm^{-2} that is suggested to be the optimal operating range for industrial applications.[12,49] The stability of DRY/20% PTFE/30min was further evaluated in the flow cell at 200 mA cm^{-2}, as shown in Fig. S14.† Through 12 h of electrochemical testing the selectivity of C_2H_4 production remained stable at around 43% and that of H_2 was also stably low at around 8%. This stability matches other top performing literature reports tested at similar current densities.[26,29,32,50] Considering that the use of commercial Cu NPs usually leads to lower catalytic performance than lab-synthesized Cu nanocrystals,[31,35] the high performance of DRY/20%PTFE/30min catalyst manufactured from commercial Cu and PTFE powders in this work has made a breakthrough for commercial Cu based catalysts.

The significantly increased selectivity for C_{2+} products of the DRY/20%PTFE/30min compared to WET/20%PTFE could be credited to the almost complete coating of porous PTFE on Cu that increased the PTFE–Cu interfacial area in the solid–liquid–gas triphase region and facilitated CO_2 transport, as well as the increased hydrophobicity of the catalyst that changed the microenvironment of the catalyst layer.[33,44,47,48] The variance in performance of the DRY prepared cathodes depending on PTFE mass loading and ball milling time could be mainly attributed to the varied degree of PTFE coverage on Cu (Fig. S6 and S7†), since all the DRY samples had very similar measured water contact angles (Table S1†). First, the higher the PTFE loading up to the optimal level of 20% PTFE, the higher the CO_2RR performance. However, when the PTFE loading exceeds the optimal (*e.g.* 35% PTFE), the CO_2RR performance decreases because of the insulation nature of the PTFE and the possible blockage of CO_2 passage due to too dense of a PTFE overcoating (Fig. S7†). Second, the longer the ball milling time, the higher the CO_2RR performance, as it takes time to form a complete

Published on 20 November 2023. Downloaded by Texas A & M University on 6/3/2024 5:10:04 PM.

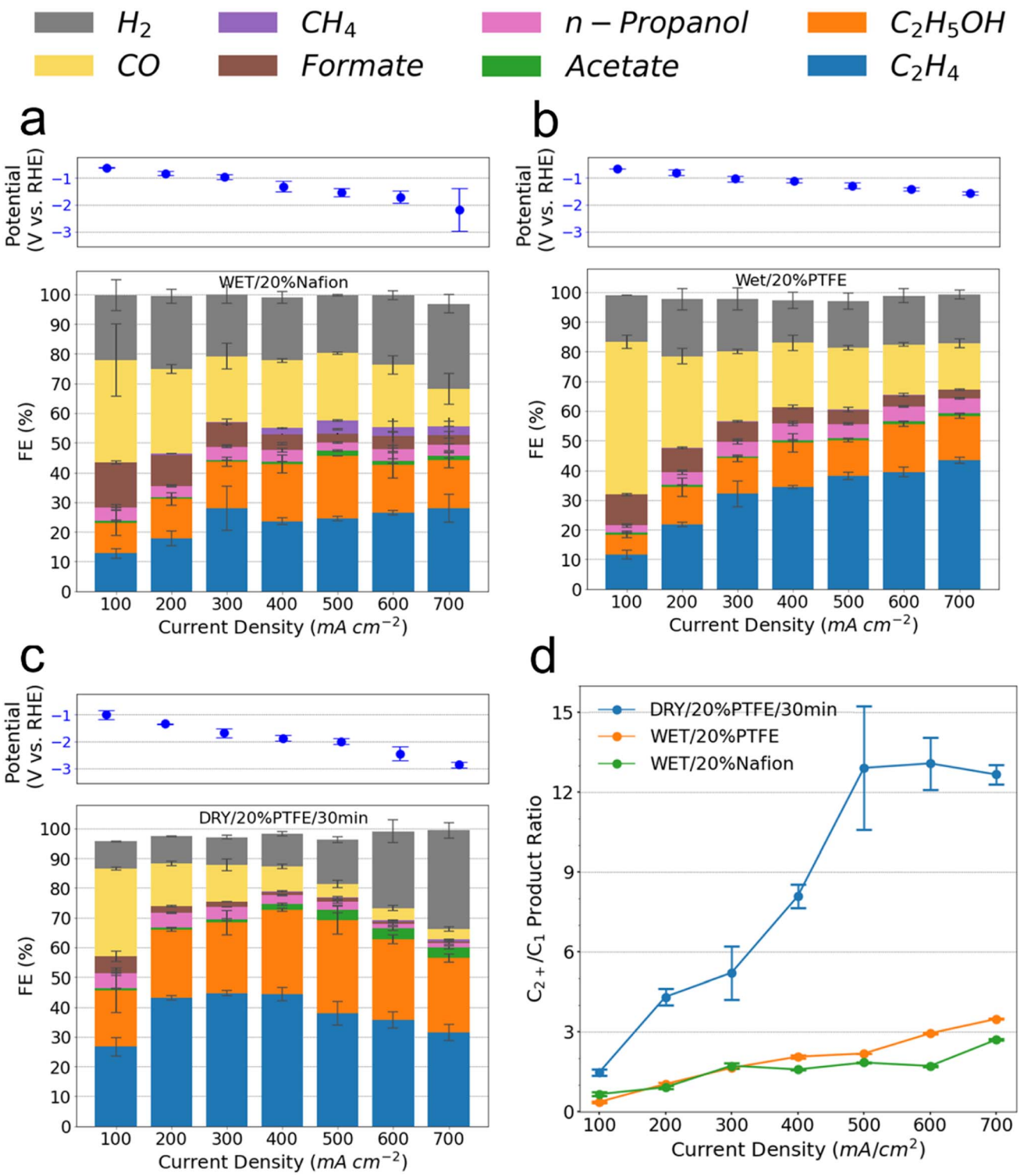

Fig. 5 Comparison of electrochemical performances of DRY and WET samples (a) WET/20%Nafion, (b) WET/20%PTFE, (c) DRY/20%PTFE/30min regarding faradaic efficiency and working potential over a range of applied current densities, and (d) comparison of C_{2+}/C_1 product ratios between DRY/20%PTFE/30min, WET/20%PTFE, and WET/20%Nafion over a range of applied current densities.

PTFE coating on Cu. However, when exceeding the optimal level (30 min), a longer time does not further improve the CO_2RR performance but rather increases the energy consumption of the synthesis process.

DFT calculations

To better understand the enhanced selectivity to C_{2+} products of DRY/20%PTFE/30min catalyst, the first principles DFT calculations were performed to predict the free energy evolution

 This journal is © The Royal Society of Chemistry 2023

Published on 20 November 2023. Downloaded by Texas A & M University on 6/3/2024 5:10:04 PM.

along different CO_2RR pathways (see ESI† Computational details). Since (100) and (111) surfaces were reported as the primary facets of Cu catalysts to promote CO_2/CO reduction in both experiments and simulations,[51–54] we investigated specifically how the PTFE coating would modify the pathway of CO_2 reduction on these two surfaces. In this study, we considered two types of adsorption configurations for PTFE onto the surface of Cu, namely physical adsorption configuration in which a PTFE chain is adsorbed parallelly on the surface (Fig. 6a and S15b†) and chemical adsorption configuration in which a PTFE chain is adsorbed perpendicularly on the surface (Fig. S15a†).

To examine the optimal adsorption configuration of PTFE on Cu surface, we have calculated and compared the adsorption energies of the two adsorption configurations consisting of Cu surface and a short $(CF_2)_4$ chain (Fig. S15†). In this study as a simplification in the DFT calculations, we used a monomer of CF_2 adsorbed on Cu surface to model the chemical adsorption of PTFE on Cu (Fig. 6b). We predicted the adsorption energy of PTFE on Cu(111) surface to be −1.71 eV with a perpendicular adsorption configuration (*i.e.*, chemical adsorption) and −0.32 eV with a parallel adsorption configuration (*i.e.*, physical adsorption). The chemical adsorption was more energetically favorable than the physical adsorption, agreeing well with previous conclusions.[55,56]

Next, we constructed six computational models including (a) clean Cu(100), (b) Cu(100) with chemically adsorbed PTFE (cPTFE-Cu(100)), (c) Cu(100) with physically adsorbed PTFE (pPTFE-Cu(100)), (d) clean Cu(111), (e) Cu(111) with chemically adsorbed PTFE (cPTFE-Cu(111)) and (f) Cu(111) with physically adsorbed PTFE (pPTFE-Cu(111)), as shown in Fig. S16.† Models (a) and (d), clean Cu surfaces, are used to represent WET catalysts where PTFE NPs are simply mixed with Cu NPs (Fig. 1a), while the remaining four models are used to represent DRY catalysts where Cu NPs are covered by a PTFE nanocoating (Fig. 1b).

A good catalyst for CO_2 reduction to C_{2+} products should meet at least two criteria: (1) adequate adsorption energy for CO and (2) feasible activation energy for C–C coupling. Consequently, we examined how PTFE would affect the CO adsorption on Cu surfaces. It should be noted that a more negative value of CO adsorption energy shows stronger adsorption of CO onto the Cu surface. Our DFT calculations predicted the CO adsorption energies to be −0.47, −0.48, and −0.51 eV on clean Cu(111), cPTFE-Cu(111), and pPTFE-Cu(111) surfaces, respectively (Table S9†). In addition, we found that the CO adsorption on Cu(100) was also strengthened by PTFE. These results indicate that the introduction of PTFE, especially *via* physical adsorption, could strengthen the binding of CO on Cu and hence hinder the desorption of CO from the PTFE-decorated Cu surface. Thus, our predictions well explain the experimental observation that the faradaic efficiency for undesired CO production at 400 mA cm^{-2} decreased from 21% in WET/20%PTFE catalyst to 9% in DRY/20%PTFE/30min catalyst (Fig. 5b and c).

Moreover, we investigated how PTFE would affect the free energy change for C–C coupling process, which is critical to the formation of C_2 products.[57] In this study, we examined two possible processes, namely the CO–CO and CO–CHO coupling

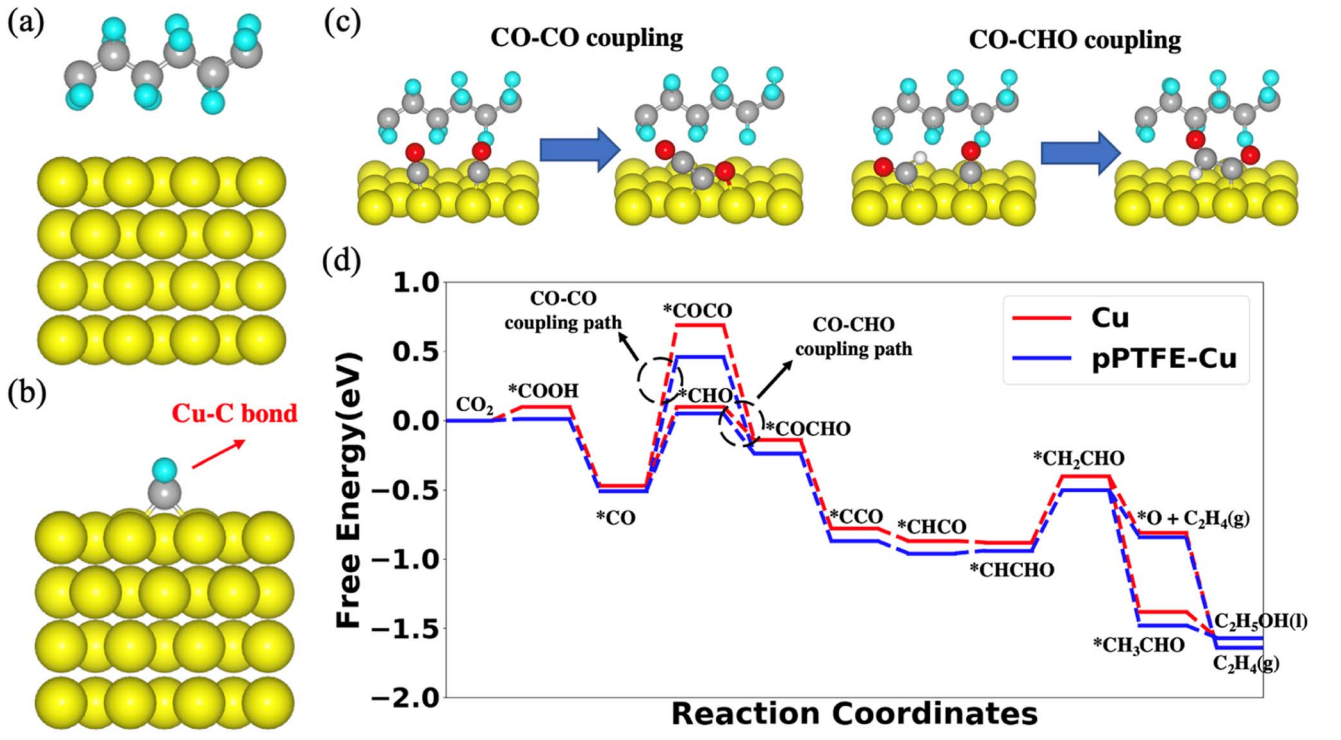

Fig. 6 Atomistic structures of (a) physical adsorption configuration of PTFE on Cu(111), (b) chemical adsorption configuration of PTFE on Cu(111), and (c) the CO–CO and CO–CHO coupling process. Here, the yellow, grey, cyan, red, and white balls represent Cu, C, F, O, and H atoms, respectively. (d) Predicted free energy evolution for CO_2 reduction to C_2 products on clean Cu(111) and pPTFE-Cu(111) surfaces.

Published on 20 November 2023. Downloaded by Texas A & M University on 6/3/2024 5:10:04 PM.

processes (Fig. 6c). We predicted that it required to overcome at least 0.71 eV of free energy change for the CO–CO coupling step on all the modelled Cu surfaces (Table S9†). In contrast, the free energy change for the CO–CHO coupling step was predicted to be negative on these surfaces. These results suggest that the CO–CHO coupling process is energetically more favorable than the CO–CO coupling process on Cu surfaces. Furthermore, we performed the nudged elastic band calculations[58] to predict the activation energy required for the CO–CHO coupling step. As shown in Table S9,† the activation energy for the CO–CHO coupling was predicted to be 0.83 eV on clean Cu(111), 0.82 eV on cPTFE-Cu (111), and 0.78 eV on pPTFE-Cu(111). We also predicted that the activation energy for the CO–CHO coupling step would decrease from 0.65 eV on clean Cu(100) surface to 0.60 eV on pPTFE-Cu(100) surface. These results reveal that the addition of PTFE could accelerate the CO–CHO coupling step on Cu catalyst surfaces and the physically adsorbed PTFE shows a better capability than the chemically adsorbed PTFE to promote the CO–CHO coupling.

We ascribed the enhancement in the adsorption of CO_2 reduction intermediates on pPTFE-Cu(111) surface to be the steric effect. Many studies have reported that the energy of a chemical species on a surface was not only affected by the electronic structure of the surface, but also influenced by the steric effect.[59–61] Illustrating how the PTFE coating affects the electron structure of Cu surface, we have performed DFT calculations and Bader charge analysis to calculate the electron density of Cu atoms on Cu(111) surface with and without physically adsorbed PTFE.[62] As shown in Table S10,† we found that the introduction of physically adsorbed PTFE molecule would have neglectable change on the electron density (from 11 to 10.996 $|e|$/Cu atom) of Cu surface atoms. This result indicates that the physically adsorbed PTFE would not change the electron structure of Cu. We used a *COCHO intermediate as an example to illustrate the steric effect in our pPTFE-Cu(111) model. As shown in Fig. S17,† the physically adsorbed PTFE would cause a slight rotation of *COCHO on Cu surface to form a hydrogen bonding interaction between the H in *COCHO and the F in PTFE. This hydrogen bond is predicted to reduce the system energy and thus affects the reaction pathway (as shown in Fig. 6d). Hence, we believe that incorporation of physically adsorbed PTFE could change the reaction pathway *via* the steric effect rather than by changing the electron density of Cu.

Regarding the physically adsorbed PTFE showing more pronounced effect on inhibiting CO desorption and promoting C–C coupling on Cu surfaces, we compared the free energy evolution for CO_2 reduction to C_2 products on Cu(111) and pPTFE-Cu(111) surface (Fig. 6d). We predicted that the introduction of PTFE could enhance the adsorption of each intermediate and lead to the potential determining step of CO to CHO and the CO–CHO coupling step to be more favorable. Consequently, the addition of PTFE polymer was predicted to enhance both the activity and selectivity for CO_2 reduction to C_2 products on Cu, consistent with our experimental finding that DRY/20%PTFE/30min catalyst exhibits a C_{2+}/C_1 product ratio of 13 much higher than the value of 2 for the WET/20%PTFE catalyst at 400 mA cm^{-2} (Fig. 5d).

Conclusion

In summary, a novel DRY manufacturing method has been developed for preparing micro-granule catalysts composed of Cu NPs coated by porous PTFE nanofilm. These micro-granules were then deposited onto a GDL through electrostatic deposition and roll pressing to form a GDE in a solvent-free process. The preparation parameters including PTFE mass loading and ball milling time are important to affect the Cu–PTFE granulation and the PTFE coating uniformity, and consequently the CO_2RR performance. Specifically, the optimal sample, DRY/20%PTFE/30min, achieved an FE (C_{2+}) of 78% at 400 mA cm^{-2} and an FE (C_{2+}) of 76% at 500 mA cm^{-2} with a large C_{2+} to C_1 product ratio of 13, significantly higher than those catalysts prepared by conventional WET methods airbrushing catalyst ink composed of Cu NPs and PTFE or Nafion binder. The DRY sample also demonstrated excellent stability for 12 h without observable degradation of FE (C_{2+}). Besides the contributions from the porous PTFE layer that promoted the catalyst–electrode–CO_2 interfacial area and GDE hydrophobicity, our DFT results indicated that a physisorbed PTFE polymer layer could hinder the desorption of CO from PTFE-covered Cu surfaces while accelerating the C–C coupling step on the same surface. This work not only provides useful insights of a new materials structure for high-performing CO_2RR catalysts but also demonstrates the potential for scalable and sustainable manufacturing of the catalysts, both of which are critical to large-scale CO_2RR applications. Future work could focus on improving the PTFE coating techniques and fabricating smaller granules to minimize the decrease in ECSA and further increase catalytic performance.

Author contributions

Y. Li and H. Pan conceived the research idea, guided the research direction, and managed the research project and manuscript writing. J. Pellessier, Y. Gang, and K. Hambleton performed experiments of electrochemical CO_2 reduction and data analysis. J. Pellessier, X. Gong, and Y. Gang performed materials and electrode synthesis and characterization including XRD, XPS, and water contact angle. J. Zhang and H. Zhou performed TEM and BET analyses. B. Li and G. Wang performed DFT calculations. C. Podder and Z. Gao performed the FIB, SEM and EDS mapping. J. Pellessier, X. Gong, and B. Li wrote the manuscript. Y. Li, H. Pan, and G. Wang revised the manuscript.

Conflicts of interest

There are no conflicts to declare.

Acknowledgements

This work was supported by the U.S. National Science Foundation (NSF CBET #1805132, CBET #1804534, CMMI #2054098, and DMR #1905572). The authors acknowledge that part of the characterization work was performed in the Texas A & M

 This journal is © The Royal Society of Chemistry 2023

Published on 20 November 2023. Downloaded by Texas A & M University on 6/3/2024 5:10:04 PM.

University Materials Characterization Core Facility (RRID:SCR_022202) and the Texas A & M University Microscopy & Imaging Center (RRID:SCR_022128). This research was also supported in part by the University of Pittsburgh Center for Research Computing (RRID:SCR_022735) through the computer resources provided. Specifically, this work used the H2P cluster, which is supported by NSF award number OAC-2117681.

References

1 F. H. Saadi, N. S. Lewis and E. W. McFarland, *Energy Environ. Sci.*, 2018, **11**, 469–475.
2 L. Fan, C. Xia, F. Yang, J. Wang, H. Wang and Y. Lu, *Sci. Adv.*, 2020, **6**, eaay3111.
3 Y. Wang, C. Li, Z. Fan, Y. Chen, X. Li, L. Cao, C. Wang, L. Wang, D. Su, H. Zhang, T. Mueller and C. Wang, *Nano Lett.*, 2020, **20**, 8074–8080.
4 F. Pan, B. Li, W. Deng, Z. Du, Y. Gang, G. Wang and Y. Li, *Appl. Catal., B*, 2019, **252**, 240–249.
5 F. Pan, B. Li, E. Sarnello, S. Hwang, Y. Gang, X. Feng, X. Xiang, N. M. Adli, T. Li, D. Su, G. Wu, G. Wang and Y. Li, *Nano Energy*, 2020, **68**, 104384.
6 J. Pellessier, Y. Gang and Y. Li, *ES Mater. Manuf.*, 2021, **13**, 66–75.
7 Y. Gang, E. Sarnello, J. Pellessier, S. Fang, M. Suarez, F. Pan, Z. Du, P. Zhang, L. Fang, Y. Liu, T. Li, H.-C. Zhou, Y. H. Hu and Y. Li, *ACS Catal.*, 2021, **11**, 10333–10344.
8 Y. Gang, F. Pan, Y. Fei, Z. Du, Y. H. Hu and Y. Li, *ACS Sustainable Chem. Eng.*, 2020, **8**, 8840–8847.
9 T. Möller, W. Ju, A. Bagger, X. Wang, F. Luo, T. N. Thanh, A. S. Varela, J. Rossmeisl and P. Strasser, *Energy Environ. Sci.*, 2019, **12**, 640–647.
10 H. Yang, Q. Lin, C. Zhang, X. Yu, Z. Cheng, G. Li, Q. Hu, X. Ren, Q. Zhang, J. Liu and C. He, *Nat. Commun.*, 2020, **11**, 593.
11 Q. Fan, P. Hou, C. Choi, T.-S. Wu, S. Hong, F. Li, Y.-L. Soo, P. Kang, Y. Jung and Z. Sun, *Adv. Energy Mater.*, 2020, **10**, 1903068.
12 M. G. Kibria, J. P. Edwards, C. M. Gabardo, C. T. Dinh, A. Seifitokaldani, D. Sinton and E. H. Sargent, *Adv. Mater.*, 2019, **31**, 1807166.
13 M. Jouny, W. Luc and F. Jiao, *Ind. Eng. Chem. Res.*, 2018, **57**, 2165–2177.
14 J. Albero, Y. Peng and H. García, *ACS Catal.*, 2020, **10**, 5734–5749.
15 M. B. Gawande, A. Goswami, F.-X. Felpin, T. Asefa, X. Huang, R. Silva, X. Zou, R. Zboril and R. S. Varma, *Chem. Rev.*, 2016, **116**, 3722–3811.
16 A. Bagger, W. Ju, A. S. Varela, P. Strasser and J. Rossmeisl, *ACS Catal.*, 2019, **9**, 7894–7899.
17 S. Zhu, E. P. Delmo, T. Li, X. Qin, J. Tian, L. Zhang and M. Shao, *Adv. Mater.*, 2021, **33**, 2005484.
18 Y. Wang, J. Liu and G. Zheng, *Adv. Mater.*, 2021, **33**, 2005798.
19 H. Mistry, A. S. Varela, C. S. Bonifacio, I. Zegkinoglou, I. Sinev, Y.-W. Choi, K. Kisslinger, E. A. Stach, J. C. Yang, P. Strasser and B. R. Cuenya, *Nat. Commun.*, 2016, **7**, 12123.
20 C. Xiao and J. Zhang, *ACS Nano*, 2021, **15**, 7975–8000.
21 D. Karapinar, C. E. Creissen, J. G. Rivera de la Cruz, M. W. Schreiber and M. Fontecave, *ACS Energy Lett.*, 2021, **6**, 694–706.
22 Y. Chen, Z. Fan, J. Wang, C. Ling, W. Niu, Z. Huang, G. Liu, B. Chen, Z. Lai, X. Liu, B. Li, Y. Zong, L. Gu, J. Wang, X. Wang and H. Zhang, *J. Am. Chem. Soc.*, 2020, **142**, 12760–12766.
23 C. Choi, T. Cheng, M. Flores Espinosa, H. Fei, X. Duan, W. A. Goddard III and Y. Huang, *Adv. Mater.*, 2019, **31**, 1805405.
24 C. Choi, S. Kwon, T. Cheng, M. Xu, P. Tieu, C. Lee, J. Cai, H. M. Lee, X. Pan, X. Duan, W. A. Goddard and Y. Huang, *Nat. Catal.*, 2020, **3**, 804–812.
25 Z. Gu, H. Shen, Z. Chen, Y. Yang, C. Yang, Y. Ji, Y. Wang, C. Zhu, J. Liu, J. Li, T.-K. Sham, X. Xu and G. Zheng, *Joule*, 2021, **5**, 429–440.
26 Y. Ma, J. Yu, M. Sun, B. Chen, X. Zhou, C. Ye, Z. Guan, W. Guo, G. Wang, S. Lu, D. Xia, Y. Wang, Z. He, L. Zheng, Q. Yun, L. Wang, J. Zhou, P. Lu, J. Yin, Y. Zhao, Z. Luo, L. Zhai, L. Liao, Z. Zhu, R. Ye, Y. Chen, Y. Lu, S. Xi, B. Huang, C.-S. Lee and Z. Fan, *Adv. Mater.*, 2022, **34**, 2110607.
27 A. Herzog, A. Bergmann, H. S. Jeon, J. Timoshenko, S. Kühl, C. Rettenmaier, M. Lopez Luna, F. T. Haase and B. Roldan Cuenya, *Angew. Chem., Int. Ed.*, 2021, **60**, 7426–7435.
28 H. Jia, Y. Yang, T. H. Chow, H. Zhang, X. Liu, J. Wang and C.-y. Zhang, *Adv. Funct. Mater.*, 2021, **31**, 2101255.
29 G. L. De Gregorio, T. Burdyny, A. Loiudice, P. Iyengar, W. A. Smith and R. Buonsanti, *ACS Catal.*, 2020, **10**, 4854–4862.
30 Q. He, D. Liu, J. H. Lee, Y. Liu, Z. Xie, S. Hwang, S. Kattel, L. Song and J. G. Chen, *Angew. Chem., Int. Ed.*, 2020, **59**, 3033–3037.
31 Z. Xing, L. Hu, D. S. Ripatti, X. Hu and X. Feng, *Nat. Commun.*, 2021, **12**, 136.
32 X. Chen, J. Chen, N. M. Alghoraibi, D. A. Henckel, R. Zhang, U. O. Nwabara, K. E. Madsen, P. J. A. Kenis, S. C. Zimmerman and A. A. Gewirth, *Nat. Catal.*, 2021, **4**, 20–27.
33 F. P. García de Arquer, C.-T. Dinh, A. Ozden, J. Wicks, C. McCallum, A. R. Kirmani, D.-H. Nam, C. Gabardo, A. Seifitokaldani, X. Wang, Y. C. Li, F. Li, J. Edwards, L. J. Richter, S. J. Thorpe, D. Sinton and E. H. Sargent, *Science*, 2020, **367**, 661–666.
34 X. Wei, Z. Yin, K. Lyu, Z. Li, J. Gong, G. Wang, L. Xiao, J. Lu and L. Zhuang, *ACS Catal.*, 2020, **10**, 4103–4111.
35 Q. Chang, J. H. Lee, Y. Liu, Z. Xie, S. Hwang, N. S. Marinkovic, A.-H. A. Park, S. Kattel and J. G. Chen, *JACS Au*, 2022, **2**, 214–222.
36 X. Wang, S. Sahoo, J. Gascon, M. Bragin, F. Liu, J. Olchowski, S. Rothfarb, Y. Huang, W. Xiang, P.-X. Gao, S. Pamir Alpay and B. Li, *Energy Environ. Sci.*, 2023, **16**, 4388–4403.
37 M. Jun, D. Kim, M. Kim, M. Kim, T. Kwon and K. Lee, *ACS Omega*, 2022, **7**, 42655–42663.
38 S. Ahn, K. Klyukin, R. J. Wakeham, J. A. Rudd, A. R. Lewis, S. Alexander, F. Carla, V. Alexandrov and E. Andreoli, *ACS Catal.*, 2018, **8**, 4132–4142.

Published on 20 November 2023. Downloaded by Texas A & M University on 6/3/2024 5:10:04 PM.

39 S. Verma, X. Lu, S. Ma, R. I. Masel and P. J. A. Kenis, *Phys. Chem. Chem. Phys.*, 2016, **18**, 7075–7084.
40 M. Duarte, B. De Mot, J. Hereijgers and T. Breugelmans, *ChemElectroChem*, 2019, **6**, 5596–5602.
41 C.-T. Dinh, T. Burdyny, M. G. Kibria, A. Seifitokaldani, C. M. Gabardo, F. P. G. D. Arquer, A. Kiani, J. P. Edwards, P. D. Luna, O. S. Bushuyev, C. Zou, R. Quintero-Bermudez, Y. Pang, D. Sinton and E. H. Sargent, *Science*, 2018, **360**, 783–787.
42 G. Liu, D. McLaughlin, S. Thiele and C. Van Pham, *Chem. Eng. J.*, 2023, **460**, 141757.
43 J. Wang, T. Cheng, A. Q. Fenwick, T. N. Baroud, A. Rosas-Hernández, J. H. Ko, Q. Gan, W. A. Goddard III and R. H. Grubbs, *J. Am. Chem. Soc.*, 2021, **143**, 2857–2865.
44 P. An, L. Wei, H. Li, B. Yang, K. Liu, J. Fu, H. Li, H. Liu, J. Hu, Y.-R. Lu, H. Pan, T.-S. Chan, N. Zhang and M. Liu, *J. Mater. Chem. A*, 2020, **8**, 15936–15941.
45 M. C. Biesinger, L. W. M. Lau, A. R. Gerson and R. S. C. Smart, *Appl. Surf. Sci.*, 2010, **257**, 887–898.
46 P. Iyengar, M. J. Kolb, J. R. Pankhurst, F. Calle-Vallejo and R. Buonsanti, *ACS Catal.*, 2021, **11**, 4456–4463.
47 R. Chen, H. Y. Su, D. Liu, R. Huang, X. Meng, X. Cui, Z. Q. Tian, D. H. Zhang and D. Deng, *Angew. Chem., Int. Ed.*, 2020, **59**, 154–160.
48 A. Wagner, C. D. Sahm and E. Reisner, *Nat. Catal.*, 2020, **3**, 775–786.
49 J.-D. Yi, X. Gao, H. Zhou, W. Chen and Y. Wu, *Angew. Chem., Int. Ed.*, 2022, **61**, e202212329.
50 J. Zhang, W. Luo and A. Züttel, *J. Mater. Chem. A*, 2019, **7**, 26285–26292.
51 F. Calle-Vallejo and M. T. Koper, *Angew. Chem.*, 2013, **125**, 7423–7426.
52 Q. Zhao, J. M. P. Martirez and E. A. Carter, *Proc. Natl. Acad. Sci. U. S. A.*, 2022, **119**, e2202931119.
53 Y. Wang, H. Shen, K. J. Livi, D. Raciti, H. Zong, J. Gregg, M. Onadeko, Y. Wan, A. Watson and C. Wang, *Nano Lett.*, 2019, **19**, 8461–8468.
54 B. Hagman, A. Posada-Borbón, A. Schaefer, M. Shipilin, C. Zhang, L. R. Merte, A. Hellman, E. Lundgren, H. Grönbeck and J. Gustafson, *J. Am. Chem. Soc.*, 2018, **140**, 12974–12979.
55 J. Wu, X. Wang, H. Li, F. Wang, W. Yang and Y. Hu, *Nano Energy*, 2018, **48**, 607–616.
56 L. Wang, Y. Dong, J. Tao, T. Ma and Z. Dai, *J. Phys. D: Appl. Phys.*, 2020, **53**, 285302.
57 J. D. Goodpaster, A. T. Bell and M. Head-Gordon, *J. Phys. Chem. Lett.*, 2016, **7**, 1471–1477.
58 G. Henkelman, B. P. Uberuaga and H. Jonsson, *J. Chem. Phys.*, 2000, **113**, 9901–9904.
59 X. Chen, Y. Dai, H. Zhang and X. Zhao, *Colloids Surf., A*, 2023, **663**, 131091.
60 K. C. Harper and M. S. Sigman, *Science*, 2011, **333**, 1875–1878.
61 G. Lu, R. Y. Liu, Y. Yang, C. Fang, D. S. Lambrecht, S. L. Buchwald and P. Liu, *J. Am. Chem. Soc.*, 2017, **139**, 16548–16555.
62 E. Sanville, S. D. Kenny, R. Smith and G. Henkelman, *J. Comput. Chem.*, 2007, **28**, 899–908.

 This journal is © The Royal Society of Chemistry 2023